mmWall: A Steerable, Transflective Metamaterial Surface for NextG mmWave Networks

Kun Woo Cho, *Princeton University;* Mohammad H. Mazaheri, *UCLA;*
Jeremy Gummeson, *University of Massachusetts Amherst;*
Omid Abari, *UCLA;* Kyle Jamieson, *Princeton University*

https://www.usenix.org/conference/nsdi23/presentation/cho-kun-woo

This paper is included in the
Proceedings of the 20th USENIX Symposium on
Networked Systems Design and Implementation.

April 17–19, 2023 • Boston, MA, USA

978-1-939133-33-5

Open access to the Proceedings of the
20th USENIX Symposium on Networked
Systems Design and Implementation
is sponsored by

جامعة الملك عبدالله
للعلوم والتقنية
King Abdullah University of
Science and Technology

mmWall: A Steerable, Transflective Metamaterial Surface for NextG mmWave Networks

Kun Woo Cho[1], Mohammad H. Mazaheri[3], Jeremy Gummeson[2], Omid Abari[3], Kyle Jamieson[1]
Princeton Univ.[1], Univ. of Massachusetts Amherst[2], UCLA[3]

Abstract

Mobile operators are poised to leverage millimeter wave technology as 5G evolves, but despite efforts to bolster their reliability indoors and outdoors, mmWave links remain vulnerable to blockage by walls, people, and obstacles. Further, there is significant interest in bringing outdoor mmWave coverage indoors, which for similar reasons remains challenging today. This paper presents the design, hardware implementation, and experimental evaluation of *mmWall*, the first electronically almost-360° steerable metamaterial surface that operates above 24 GHz and both refracts or reflects incoming mmWave transmissions. Our metamaterial design consists of arrays of varactor-split ring resonator unit cells, miniaturized for mmWave. Custom control circuitry drives each resonator, overcoming coupling challenges that arise at scale. Leveraging beam steering algorithms, we integrate mmWall into the link layer discovery protocols of common mmWave networks. We have fabricated a 10 cm by 20 cm mmWall prototype consisting of a 28 by 76 unit cell array and evaluated it in indoor, outdoor-to-indoor, and multi-beam scenarios. Indoors, mmWall guarantees 91% of locations outage-free under 128-QAM mmWave data rates and boosts SNR by up to 15 dB. Outdoors, mmWall reduces the probability of complete link failure by a ratio of up to 40% under 0–80% path blockage and boosts SNR by up to 30 dB.

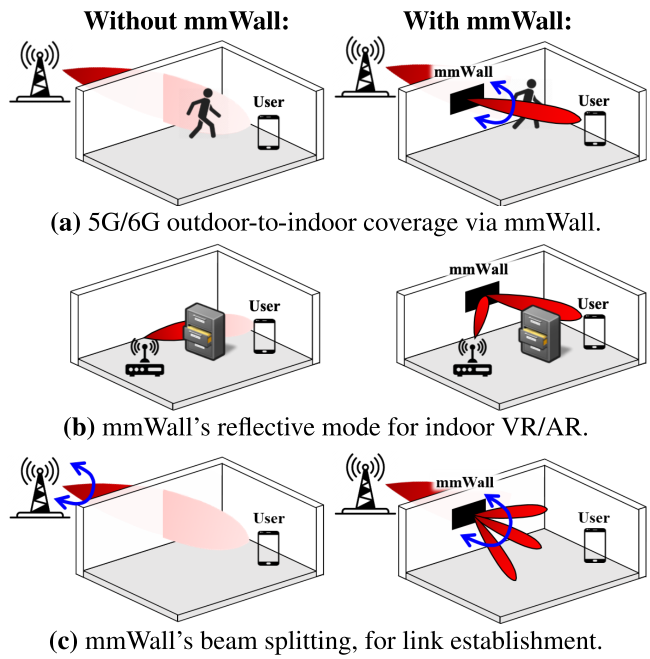

Figure 1: mmWall re-focuses outdoor coverage indoors towards the user and potentially around obstacles, provides path diversity indoors by reflection, and splits an incoming beam for fast link establishment.

1 Introduction

Millimeter-wave (mmWave) spectrum has emerged in the 5G/6G era as a key next generation wireless network enabler, fulfilling user demands for high spectral efficiency and low latency wireless networks. Higher carrier frequencies offer greater network capacity: for instance, the maximum carrier frequency of the 4G LTE band at 2.4 GHz provides an available spectrum bandwidth of only 100 MHz, while mmWave (above 24 GHz) can easily hold spectral bandwidths five to ten times greater, enabling multi-Gbit/sec data rates. Hence, mmWave spectrum enables a plethora of mobile applications that are currently infeasible due to their requirements of very high data rates, such as virtual and augmented reality (VR/-AR), camera-based purchase tracking in smart stores, and robotic automation in smart warehouses.

mmWave technology faces significant headwinds, however, in at least three key scenarios:

1. 5G outdoor coverage is difficult to bring indoors, as exterior building walls block mmWave signal, as do outdoor windows' tinted glass (Fig. 1(a)). Attenuation at 28 GHz is *ca.* 40 dB versus 4 dB through indoor glass [44], as outdoor metalized glass coatings attenuate by 25–50 dB per layer [35]. Currently, operators are forced to offload

mmWave traffic onto lower frequencies or off their networks entirely (Wi-Fi) when users move indoors, incurring handover delay and application disruptions.

2. Indoors, people, furniture, doors, and other clutter block mmWave (Fig. 1(b)), forcing data to flow over a much less reliable reflection path. Indeed, in an extensive indoor measurement campaign at 28 GHz, MacCartney *et al.* observe a close-in best non-line of sight path loss exponent *ca.* 3, with a normally-distributed additional loss with an 11 dB variance [22]. While the resulting temporary outages are common, highly demanding applications like VR/AR streaming cannot tolerate these glitches.

3. Third, NextG cellular providers face challenges in adopting mmWave frequencies outdoors for primary service as well as wireless backhaul because mmWave signals are readily absorbed by foliage, and reflection off buildings is largely specular, constraining the angle of reflection to be equal to the angle of incidence. Measurements in New York City highlight this issue: 28 GHz data shows most links greater than 200 meters in outage [3].

This paper describes the design and implementation of ***mmWall***, an electronically reconfigurable surface that addresses all three foregoing use cases, also shown in Figure 1. Like much prior work (§2), mmWall leverages *metamaterials*, artificial composite materials engineered at a sub-wavelength scale to exhibit unique electromagnetic properties that do not exist in naturally occurring materials [17]. But mmWall is the first practical work to our knowledge to use a specific class of metamaterials capable of refracting incoming radiation with (theoretically) no loss: *Huygens* metamaterials [9, 25]. mmWall is a reconfigurable intelligent surface that uses a novel Huygens metasurface (HMS) metamaterial to reflect/refract and precisely steer incoming mmWave beams towards desired directions, thus enhancing path diversity for mmWave networks. Work has shown that surfaces that can steer incoming mmWave transmissions in this way have the potential to dramatically improve spatial multiplexing [41] and spectral efficiency [39] of networks as a whole. Hence when obstacles like a human body or outdoor foliage blocks the line of sight (LoS) or non line of sight (NLoS) paths, mmWall can often provide an alternative path that is not a simple reflection or a straight-line transmission, and hence would not otherwise exist. In the first scenario, mmWall can refract mmWave signals from outdoors to steer them directly towards an indoor receiver, making outdoor to indoor communication possible. In the second scenario above, mmWall reflects mmWave beams at non-specular angles (those for which the angle of reflection is not equal to the angle of incidence). And in the third scenario, mmWall can reflect outdoor transmissions at non-specular angles, ameliorating outdoor blockages.

mmWall is electronically reconfigurable to either reflect or refract incoming energy, allowing it to time-multiplex the different roles of each of the three above use cases without human intervention, while installed in a fixed location. Also, its multi-beam functionality (Fig. 1(c)) enables fast beam search, and support for multiple users at the same time. mmWall has no RF chain, and its electric components draw only a couple-of-hundred microwatts order of power. Consequently, it consumes much lower power compared to a conventional AP that necessitates multiple RF chains for multi-beam operations. To our knowledge, mmWall is the first surface able to achieve near-360° angular coverage (§5).

This work addresses several hardware and software design challenges that arise in the realization of such a design. Since mmWave transmissions are "pencil-beam" in nature, they work only when the transmitter's beam is perfectly aligned with the receiver's beam. To correctly steer the beam towards the receiver, we design a metamaterials-based surface that can precisely control the phases of the incoming signal, focusing signal power in a narrow beam. Secondly, since the size of meta-atom scales with its operating frequency, mmWall's meta-atoms are much smaller than the conventional antennas and therefore extremely sensitive to coupling. Hence, we not only scale the surface to mmWave frequency but also deliberately design the control lines to avoid undesirable coupling. Lastly, existing systems uses their own beam searching protocol to find the best alignment. To make mmWall compatible with different mmWave applications, we design an effective beam alignment protocol that leaves the existing systems unchanged [16].

Contributions and Results. mmWall is the first design that can arbitrarily reflect, refract, and split the mmWave beam in a nearly lossless manner. We analyze our meta-atom designs and compare them with simulation results, allowing our designs to scale to different frequencies for potential applications like Terahertz communication. To the best of our knowledge, this is the first study that theoretically analyzes and builds a working prototype of a reconfigurable Huygens metasurface at mmWave frequency. We have designed and implemented mmWall hardware with a novel control network in custom PCB, and in §5, evaluate its performance through experiments in environments matching the scenarios, we outline above. Our empirical results show that when both the AP and the client are in the same room, we can provide an SNR of 25 dB or more for all locations in a $10 \times 8m$ room, using a single mmWall surface. This SNR is sufficient to support 128-QAM in 91% of locations. Moreover, the SNR improves to 30 and 35 dB when we place two surfaces, respectively, on different walls. Finally, we show the effectiveness of mmWall in bringing outdoor mmWave networks indoors. When the AP is 6 meters away from the building, mmWall improves the SNR by up to 30 dB, providing an SNR of 20 dB or more in all locations in a room using a single surface placed on a window.

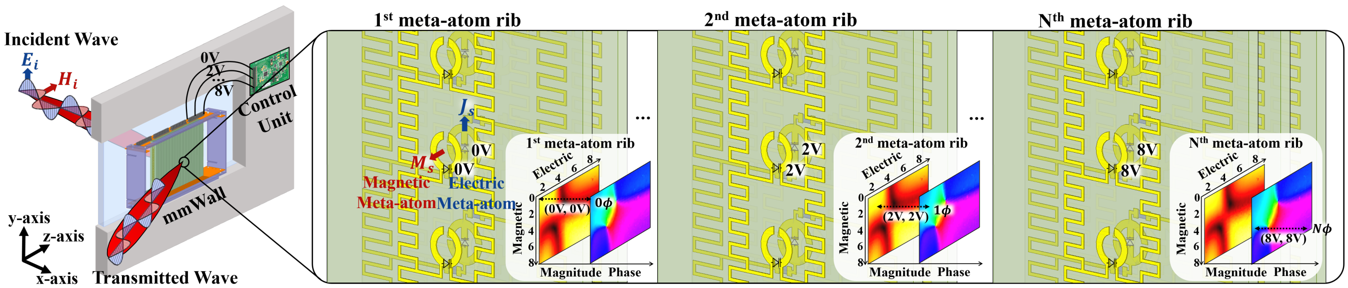

Figure 2: mmWall's design converts an incident mmWave beam to a refracted (or reflected, not shown) beam via field discontinuities created by current in its resonators. *Inset:* magnetic meta-atoms are shown in front of the electric meta-atoms.

2 Related Work

HMSs comprise a layer of co-located *magnetic* and *electric* meta-atom, etched onto the two respective sides of a dielectric substrate (Fig. 2, *inset*). The magnetic meta-atom is an enclosed metallic ring with one split, while the electric meta-atom has two splits and a metal strip in the center (Fig. 4(b)). As the incident wave passes through the magnetic meta-atom, the wave's magnetic field H_i induces a rotating current (green arrows in Fig. 4(b), *upper*) on the magnetic meta-atom that, in turn, creates a magnetic response ($\vec{M}_s$ along the z-axis in Fig. 2). Likewise, the electric meta-atom is excited by the wave's electric field $\vec{E}_i$, resulting in two symmetric, oscillating current loops (green arrows in Fig. 4(b), *lower*) that create an electric response ($\vec{J}_s$ along the y-axis in Fig. 2). These responses interact with the wave's fields, causing an abrupt phase shift. By varying the applied voltage to a tunable component loaded on each meta-atom, the surface precisely controls the responses, thereby allowing any phase shift from 0° to 360° with near-unity transmission and/or reflection.

Prior work in passive HMSs [8,9,29,40] has demonstrated a "lensing" effect and negative refraction index [29] and the engineering of complex beam patterns [8]. However, they lack the capability to reconfigure and both refract and reflect the beam. Prior work in actively-controlled HMSs [4, 7, 21, 38, 43] uses varactors or PIN diodes to tune each element in a continuous or binary (*i.e.*, on-off) manner, respectively. Such devices can shift signals' frequency [21] and polarization [5, 38]. While these designs have shown great promise in theoretical prediction models [23] and/or at low frequencies [36], they do not scale to higher mmWave frequencies in a straightforward way, due to a mismatch between the required meta-atom size and a varactor's size, and the attenuation that commonly available substrate would induce on an incident mmWave signal. Scaling these designs also requires narrower trace widths that are hard to fabricate and prone to breaking during diode soldering. More importantly, they focus on steering one beam in a one-sided direction, rather than steering one or more beams in a reflective and/or transmissive direction. mmWall is the first mmWave work to do so. Evaluation efforts in this group of prior work stop short of realistic end-to-end experiments.

Work in actively-controlled mmWave Reconfigurable Intelligent Surfaces (RISs) includes a solely reflective, PIN-diode based surface at 2.3 and 28 GHz [7], whose evaluation at 28 GHz states a gain of 19 dBi, but which stops short of further experimental evaluation of steerability or any further end-to-end evaluation at 28 GHz. Tang *et al.* describe similar PIN-diode, reflective surfaces at 27 and 33 GHz, model path losses in such scenarios, and experimentally evaluate [33]. Tan *et al.* consider a similar design at 60 GHz [31], but neither consider HMS-based designs such as mmWall's, which can shift between reflective (on both sides of the surface) and transmissive modes instantly via electronic control. Existing reflective RISs only reflect on one side, while mmWall performs both indoor *and* outdoor non-specular reflections from a fixed location. In press releases ([a], [b], [c]) NTT DoCoMo describe reflective, outdoor-to-indoor surfaces operating at 28 GHz. They state top line experimental results, but do not disclose design details or details of their experimental evaluation. Other work uses split ring resonators as antennas for a Massive MIMO base station [28], a related but distinct application to mmWall. This paper is an extension of the authors' previous workshop publication [6] that describes a new control line design, documents real hardware implementation, and presents significant new evaluation results in realistic, diverse scenarios.

Recent work in passive non-HMS based mmWave RISs includes proposals that reflect signals at angles of reflection different than incidence [11, 26], but cannot be tuned to target a receiver's location, hence wasting incident energy and resulting in at most 10 dB of gain, significantly below mmWall's achieved gain. Also, these approaches do not refract as mmWall can, yielding reduced applicability. Recent amplify-and-forward proposals for Wi-Fi [42] use a mesh topology, but do not scale to mmWave frequencies, and at mmWave [1] are limited to indoor reflection. Recent complementary approaches leverage multi-beam transmission [18, 19], sensing and leveraging ambient reflectors [37], and use Wi-Fi as a control plane to discover mmWave links [20, 30]. While they align with mmWall's goals, such approaches cannot create paths whose reflection angles diverge from their incident angles, or refract through a surface.

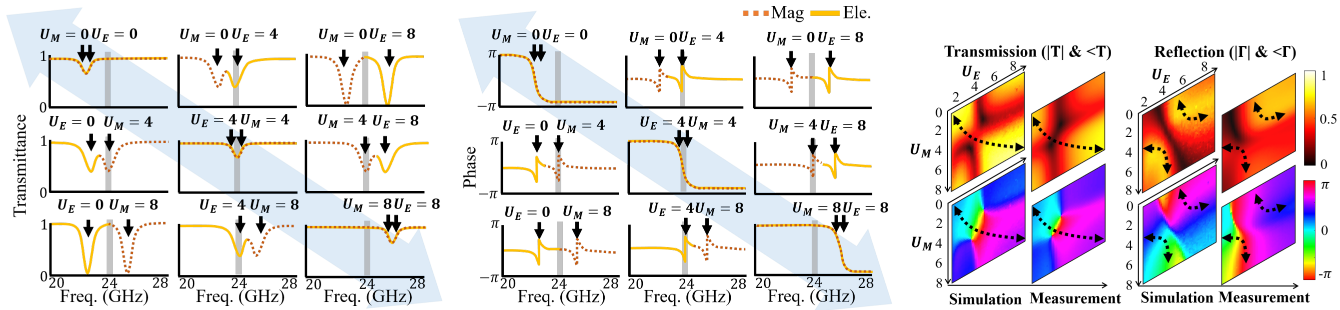

(a) Transmission magnitude $|T|$ **(b)** Transmission phase shift $\angle T$ **(c)** T and Γ magnitude, phase at 24 GHz.

Figure 3: Unit cell response *v.* electric- and magnetic-side control voltages U_E and U_M—**(a):** magnitude and **(b):** phase. **(c):** HFSS simulation (*left*) and near-field, real world VNA measurement (*right*)— arrows indicate control voltage pairs that yield a 360° phase shift of the incoming signal, with high transmission or reflection magnitude.

3 Design

We describe in turn mmWall's hardware (§3.1), their control mechanism (§3.2), and their link layer integration (§3.3).

3.1 Surface Hardware

mmWall's unit cells (also known as *meta-atoms*) are stacked vertically with a $\lambda/3$ separation, on each Rogers substrate board (also known as a *meta-atom rib*), as shown in Fig. 2 (see §3.2.1 for a discussion of vertical and horizontal unit cell spacing considerations for beamforming). A control unit connected to mmWall provides a set of voltages to the ribs. In Fig. 2, 0V is applied to both magnetic and electric meta-atoms on the first rib, causing the meta-atoms to shift the phase by 0ϕ with minimal loss. For the second rib, 2V is applied to shift the phase by 1ϕ. Ultimately, the beam is steered by all N ribs collectively forming an array factor.

3.1.1 Design Goals

The two primary design goals of the unit cell are to simultaneously **1)** achieve transmission T or reflection Γ loss levels as close to zero as possible, and **2)** effect any phase shift in $[0, 2\pi]$ on the incoming signal, both at mmWave frequencies.

The unit cell consists of two meta-atoms, *magnetic* and *electric*. The magnetic (electric) meta-atom induces a magnetic (electric) field response to the incoming signal that can resonate at different, tunable frequencies by varying the applied voltage to the varactor of the magnetic- (electric-) meta-atom.

Without loss of generality, we now describe how transmission works (reflection is fully complementary to transmission, and we refer the reader to Appendix A for a rigorous mathematical exposition of both). In Fig. 3(a), we observe that increasing the voltage applied to the magnetic meta-atom U_M from 0 to 8 V (down the three leftmost subplots) shifts its resonance frequency (lowest transmission magnitude point of the red dotted line[1]) to the right (we will analyze how this frequency shifting works in §3.1.2). Similarly, the electric meta-atom induces an electric response and its resonant frequency can be shifted by its own varactor (reading similarly across the three topmost subplots). Together their effects are superposed and we manipulate the collective magneto-electric response that interferes with the incident plane wave.

The key characteristic that allows near-perfect amplitude with full phase coverage appears when the two responses overlap at the same frequency. Otherwise, the phase response undergoes a sharp change of only π and its magnitude dips to nearly zero at its resonant frequency, as we see in Fig. 3(a) and Fig. 3(b) when the voltages applied to the magnetic and electric meta-atom differ by 8 V. However, as the two resonances start to overlap, transmission loss decreases and the phase shift becomes 2π (on-diagonal sub-figures, Fig. 3(a) and Fig. 3(b)). As a result, we achieve 2π phase coverage with near-unity magnitude by increasing the voltage applied to both the magnetic and electric meta-atoms together (Fig. 3(c), at control voltages indicated by the black curves).

While the overlapped resonances can reach a perfect unitary transmission magnitude in theory, the Huygens pattern from our measurement shows a lower transmission magnitude on the area where abrupt phase shifts occur due to various reasons, including the sensitivity at mmWave frequency, fabrication loss, and measurement errors.

3.1.2 Design Process

We now describe challenges we overcame in scaling the resonance of the mmWall unit cell to mmWave frequencies. By definition, the meta-atom behaves as an LC circuit with resonant frequency $1/(2\pi\sqrt{LC})$, determined by the capacitance or inductance of the meta-atoms. Hence, we must markedly *decrease* the inductance and capacitance of prior microwave designs (§2), if we can hope to achieve a mmWave reso-

[1] In operation we largely avoid the lowest transmission nulls.

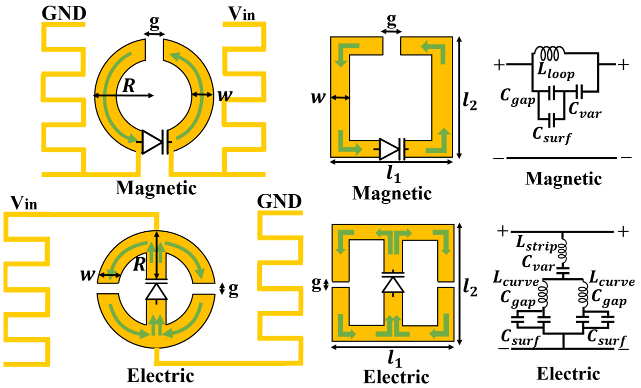

(a) mmWall **(b)** Huygens **(c)** Schematic

Figure 4: mmWall, prior Huygens unit cell designs (*top:* magnetic; *bottom:* electric side), and equivalent circuits. Green arrows indicate the oscillating current loops, and V_{in} indicates where the input voltages connect.

nant frequency. As we will see next, the smaller the ring is, the higher the resonant frequency becomes. However, the state-of-the-art approach to scale the frequency of a Huygens resonator (Fig. 4(b)) requires a loop width l_1 and loop height l_2 of $\lambda/10$. At mmWave, however, the varactor packaging itself would significantly distort the tailored electromagnetic surface properties when a meta-atom is sized $\lambda/10$, and so the straightforward approach fails. Moreover, the varactor is soldered with heat, causing tighter designs to become more fragile. Changing the rectangular cell shape to a circular one with equal diameter reduces size while preserving varactor placement on the diameter.

We thus instead adopt the design shown in Fig. 4(a), but this is only tenable with a careful tradeoff of meta-atom design parameters *radius R*, *trace width w*, and *trace gap width g* (*cf.* Fig. 4) as we next describe.

Magnetic meta-atom. Fig. 4(a) (*upper*) shows the design parameters that determine inductance L_m and capacitance C_m. L_m (= L_{loop}, the inductance of the physical conductor loop), is largely proportional to R (also $L_{\text{loop}} \propto t^{-1}$, w^{-1}, and g^{-1}). C_m consists of three capacitance values, C_{gap}, C_{surf}, and C_{var}:

$$C_m = \left(\frac{1}{C_{\text{gap}} + C_{\text{surf}}} + \frac{1}{C_{var}} \right)^{-1} \tag{1}$$

Here, C_{gap} is the parallel-plate capacitance induced by the gap in the ring ($\propto g^{-1}$), C_{surf} is a capacitance induced by the metallic surface ($\propto R$ [34]), and C_{var} is the capacitance of the varactor, a voltage-dependent capacitor. While L_{loop}, C_{gap}, and C_{surf} are fixed after fabrication, C_{var} varies with control voltage. Increasing U_M decreases C_{var} (see Fig. 17 in Appendix A for the precise relationship), and thus C_m (Eq. (1)), which in turn increases the resonance frequency, as depicted in Fig. 3.

When tuning the physical loop design parameters, we fix

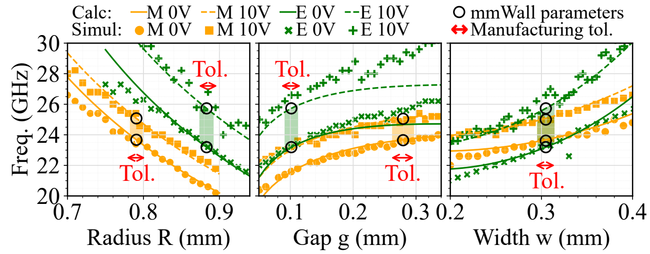

Figure 5: mmWall design parameter sensitivity analysis.

C_{var} = 4 V for both the magnetic and electric meta-atoms since at that voltage, the resonant frequency is at our desired mmWave frequency and an abrupt phase change occurs. Fig. 5 shows our chosen design parameters (denoted with black circles) and its corresponding magnetic side resonant frequency when $U_M = 0, 10$ V. Calculated (curves) and simulated (markers) data in our sensitivity analysis show that among all feature dimensions, decreasing R, followed by increasing g has the greatest effect on increasing resonant frequency for the magnetic meta-atom. We note that after fixing our meta-atom geometry as shown in the figure, 24 GHz lies in the middle of the resulting resonant frequency range. Also, we observe that PCB manufacturing tolerance (±5%) does not greatly shift the resonant frequency (we refer Appendix C for meta-atom sensitivity analysis against fabrication tolerance).

Electric meta-atom. Fig. 4(a) (*lower*) shows the electric meta-atom, in which current oscillates in two different directions, while the current of the magnetic meta-atom oscillates in one direction only (*cf.* green arrows in Figs. 4(a) and 4(b)). Hence, we analyze its inductance L_e as the combination of the inductances of the half-circular loop on the left half (L_{curve}), the inductance of the other half on the right half (L_{curve}, by symmetry), and the inductance from the metallic strip shared by two loops (L_{strip}). Since the two half-loops are arranged in parallel, with the metallic strip arranged in series, $L_e = (L_{curve}/2) + L_{strip}$ [11]. Since inductance generally depends on the surface area of the copper trace, $L_{curve} \propto R$, and $L_{strip} \propto w^{-1}$, L_e largely depends on both R and w, but not g. We see the impact of w on the resonant frequency in Fig. 5: compared to magnetic meta-atom, the resonant frequency of the electric meta-atom increases steeply as w increases due to L_{strip}. To minimize the difference in resonant frequencies between the electric and magnetic sides as desired, Fig. 5 guides us to design an electric meta-atom with equal w as the magnetic meta-atom, greater R and lesser g. The electric meta-atom has two gaps and two surface capacitances, with respective associated capacitances C_{gap} and C_{surf}, all in parallel, and that combination in series with C_{var}:

$$C_e = \left(\frac{1}{2(C_{\text{gap}} + C_{\text{surf}})} + \frac{1}{C_{\text{var}}} \right)^{-1} \tag{2}$$

Because there are many capacitances in parallel, changes in

Biasing lines—failed attempts **(a)–(c):**

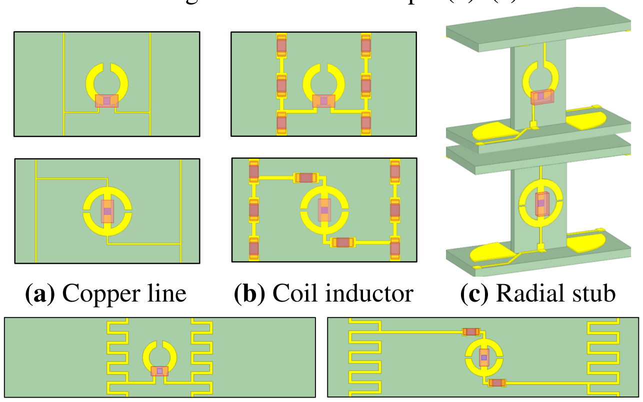

(a) Copper line **(b)** Coil inductor **(c)** Radial stub

(d) mmWall's *meander* biasing line design.

Figure 6: Biasing line designs: notable failed attempts include **(a)** straight microstrip, **(b)** coil inductor, and **(c)** radial stub. **(d)** mmWall uses an inner meander line for magnetic, and an outer meander line for electric meta-atoms.

C_{var} lead to a wider frequency shift than analogous varactor tuning of the magnetic side. Using more precise equation-based analysis (available in Appendix A) that matches our qualitative analysis, we cross-check and finalize design parameters R, g, and w for the magnetic and electric meta-atoms. We refer Appendix A.3 for the values of the design parameters and voltage distributions for different steering angles.

In Fig. 5, we observe that the difference in resonant frequencies between 0 and 10 V for the electric meta-atom are larger than the magnetic meta-atom. Hence, since the effect of C_{var} differs, overlapping of resonance will not always occur when $U_M = U_E$. Rather than of simply finding the area where $U_M = U_E$ as suggested above, we instead need to search for the voltage pair for every desired phase that also maximizes the reflection or transmission magnitude. We do this by running one-time optimization that searches for the voltage pair that maximizes $|T|$ (or $|\Gamma|$) for each phase and generates a static lookup table that will later be used for beam steering.

3.2 Surface Control

To control the meta-atoms, we connect an off-surface control unit via ribbon cables with on-surface *biasing lines*, which altogether comprise the entire *control network* (Fig. 2 on p. 3).

3.2.1 Biasing lines

This design process concerns the problem of designing the on-surface control network to interact with mmWave-frequency meta-atoms. Directly connecting a line to the meta-atoms changes the performance of the meta-atom, which causes mmWave signal loss and invalidates the design process described previously (§3.1). To mitigate such adverse effects, we seek to design biasing lines that incorporate radio frequency (RF) chokes, low pass filters that block RF signals within a certain frequency band from propagating on direct current (DC) signal paths. Our primary design goals are to design a biasing network that **1)** minimizes the use of extra components, **2)** avoids a large amount of copper on the panel where the meta-atom is placed, and **3)** is straightforward to fabricate. This is challenging because mmWave meta-atoms are sensitive to the shape and placement of the choke.

Failed attempts. Fig. 6 shows various biasing line structures we have considered. First, we try a straight copper line design **(a)**. We use a narrow width resembling a very high impedance transmission line, to try to attenuate the RF signal while the DC biasing voltage is applied. However, to achieve the desired impedance, a very narrow width transmission line (0.07 mm) is required which is not possible to fabricate by common PCB manufacturing techniques.

Second, we try the use of inductors to create a high-impedance line **(b)**. The impedance of an inductor is determined by the RF frequency and is proportional to its inductance. However, inductance of mmWave inductor components are limited. Hence, we would need to apply at least four inductors in series to achieve the desired isolation, introducing significant surface complexity and also internal resistance that adversely affects unit cell efficiency.

Third, a radial stub which is an open ended transmission line is employed. The length of the stub determines the input impedance of the line, and so thus acts as an RF "choke" that blocks mmWave signals, while a DC biasing voltage is applied to the cell from the control network. The required length of the stub is one-quarter wavelength, which is comparable to the cell size. But if the stub is designed on the same panel, the stub itself would reflect most of the wave, stealing energy to illuminate the cell itself. To avoid this problem, one can put the stubs on a perpendicular panel, as shown in Fig. 6(c). This could potentially solve the wave reflection issue, but would complicate implementation, since there would be one perpendicular panel for each unit cell.

Proposed *meander* structure. To achieve our design goals, we have formulated a meander structure (Fig. 6(d)) that acts as an RF choke, but at the same time connects the vertically adjacent meta-atoms. Longer and thinner traces provide more inductance, so by bending the straight wire vertically and horizontally, we enable the control network itself to be an inductor that outperforms the multiple off-the-shelf inductors. But this increases capacitance between the two meander lines on opposing sides of the unit cell, which also invalidates our meta-atom design process. So mmWall places the meander line of the magnetic meta-atom in a non-overlapping configuration relative to the meander line of the electric meta-atom. To compensate the loss from the microstrip that connects the electric meta-atom and the meander lines, we add two off-the-shelf inductors next to the electric meta-atom.

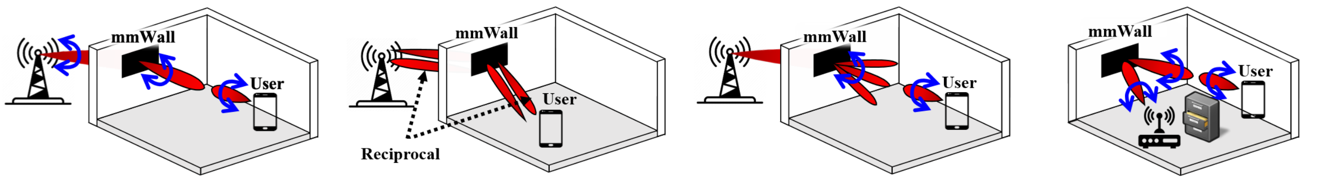

(a) Refractive establishment **(b)** Angular reciprocity **(c)** Beam tracking **(d)** Reflective establishment

Figure 7: mmWall's refractive link establishment, angular reciprocity property, tracking, and reflective link establishment.

3.2.2 Beam steering and splitting

A conventional phased array transmitter has a net radiation pattern multiplying the radiation pattern of a single element by the *array factor* (AF), the pattern induced by the array. Unlike prior mmWave receive-transmit relay systems which require two phased antenna arrays (one to receive and another to transmit a new phase-shifted signal), mmWall uses only a single array of meta-atoms to directly shift the phase of an existing mmWave signal. For L omni antennas with d separation, each with transmit amplitude A, $\mathrm{AF} = A\sum_{n=0}^{L-1} e^{2\pi jnd(\cos\theta)/\lambda}$ with radio wavelength λ and steering angle θ.

mmWall applies different phase shifts to each meta-atom rib for beam steering. Specifically, by searching over the space of control voltages to maximize reflection or transmission amplitude subject to achieving the desired phase (Fig. 3(c)), we construct a look-up table that maps steering phase φ to the chosen unit cell voltage pair (and without loss of generality) transmission coefficient: $\Phi(\varphi) \rightarrow \langle U_M, U_E, \Gamma\rangle$. The difference with conventional beamforming is that element amplitudes vary, so mmWall's net radiation pattern becomes $\sum_{n=0}^{L-1} \Phi_\Gamma(\phi)e^{j\phi}$ where $\phi = 2\pi nd\cos\theta$.

To transform a single beam into multi-armed beams, we modify the above AF to account for angles θ_1 and θ_2:

$$\sum_{n=0}^{N-1} \left(\alpha\Phi_\Gamma(\phi_1)e^{j\phi_1} + \beta\Phi_\Gamma(\phi_2)e^{j\phi_2}\right) \tag{3}$$

where $\phi_k = 2\pi nd\cos\theta_k$, and α and β are weighting terms that that determine the power of each beam.

3.3 Link Layer Design

Recall that mmWall operates in two different modes, a lens mode and a mirror mode.[2] **1)** In lens mode, a mmWave signal refracts through mmWall allowing, *e.g.*, a user inside the building to communicate with the base station (*ENodeB*) in a cellular network. This requires two beam alignments: one between the ENodeB and mmWall, and another between mmWall and the user. **2)** In mirror mode, mmWall reflects mmWave signals. For example, in wireless LAN settings, it reflects the beam between the AP and user, which requires beam alignment between the AP and mmWall, and again between mmWall and the user.

mmWall electronically switches between the two modes because different users may be located outdoors and indoors. Hence, mmWall sweeps the beam in both lens and mirror mode to align to the user during a beam search.

Our development here follows the outline of the existing 5G New Radio (NR) beam management protocol, but adapts it to mmWall's unique capabilities. The current 5G NR beam search proceeds in three steps: **1)** the ENodeB sweeps its beam, the user equipment (*UE*) selects a best direction, and reports it to the ENodeB; **2)** the ENodeB refines its beam (*i.e.*, sweeping a narrower beam over a narrower range), the user detects the best direction and reports it to the ENodeB; **3)** the ENodeB fixes a beam and the UE refines its receiver beam.

To establish a link from a cold start, the ENodeB sweeps different directions such that the user can detect the best beam for an initial link establishment (Fig. 7(a)). If the UE cannot detect the beam or the beam strength is low, it turns mmWall to a lens mode and signal it to simultaneously sweep the beam received from the ENodeB, via sub-6 GHz control. At the same time, the UE scans its receiving beam to various directions. After the search, the UE knows the combination of the ENodeB's transmit beam angle, mmWall's beam refraction angle, and its receive beam angle that maximizes the SNR of downlink signals. Given an initial link, ENodeB and mmWall refine the beam by simultaneously sweeping narrower beams over narrower ranges, and lastly, the user refines its receiving beam.[3] ENodeB-mmWall alignment takes $O(n)$ steps (for n directions), and mmWall-UE alignment takes $O(n^2)$ steps, so cold-start beam alignment as described above takes $O(n^3)$ steps, but only once *ever* when mmWall is installed, because both ENodeB and mmWall are stationary. As long as mmWall remains in the same location, the one-time initial beam alignment is kept constant. Hence, the common case of cold-start beam establishment between mmWall and user in fact requires $O(n^2)$ steps (*cf.* Fig. 7(c)). Also, the above notably does not require modifications to the existing 5G NR protocols.

As illustrated in Fig. 7(b) and demonstrated experimentally in §5.4, mmWall refracts beams in one direction at the same angle as they arrive at the surface from the other side of the

[2]Reflective mode and mirror mode are equivalent.

[3]We note that some full-duplex relays [1] require the relay node's receive direction aligned to the ENodeB, which is not necessary with mmWall.

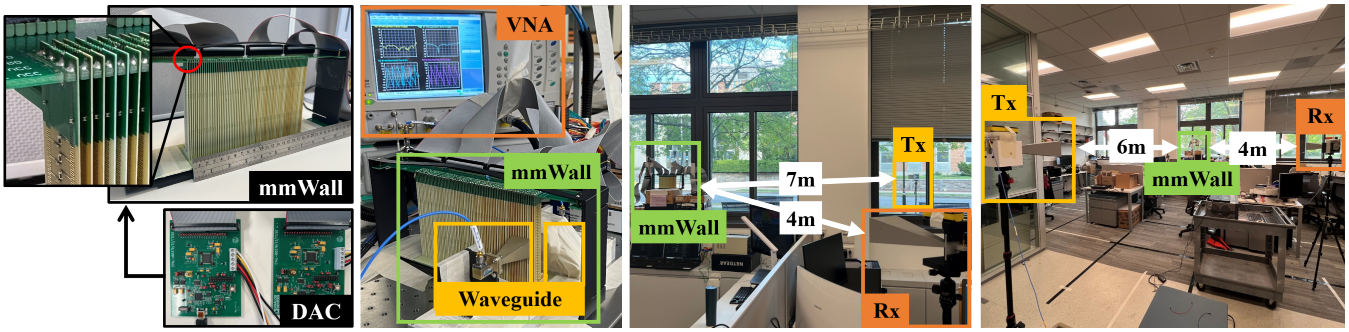

(a) mmWall hardware **(b)** Near-field testing **(c)** Outdoor-to-indoor scenario **(d)** Indoor reflective scenario

Figure 8: mmWall's hardware implementation, transmissive ('lens') and indoor reflective ('mirror') evaluation scenarios. We placed mmWall at the same location for both scenarios.

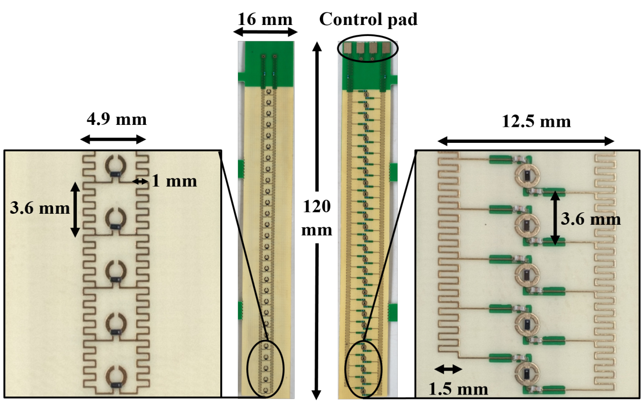

Figure 9: mmWall's *ribs*, comprised of our proposed meta-atom design fabricated on a Rogers printed circuit board.

surface (angular reciprocity), which obviates the need for separate downlink and uplink link establishment. If the downlink has already been established, mmWall does not reconfigure for the uplink. Instead, EnodeB simply switches the direction of its receiving beam to match its transmit beam, and the user transmits in the direction of its receiving beam. This facilitates a quick transition between downlink and uplink.

Since the UE controls mmWall, the user can alternate between the 'lens' mode for outdoor-to-indoor communication and the 'mirror' mode for indoor communication. For example, when the user switches from an outdoor to an indoor ENodeB, it signals mmWall to re-establish the beam estimation process for indoor usage.

Multi-beam search. mmWall can create irregular beam shapes such as multi-arm beams (§5.3), which allows it to leverage state-of-the-art beam searching algorithms that exploit the sparsity of the mmWave channel to accelerate beam search [2, 27] by orders of magnitude improvement (essential for agile and mobile applications such as VR), now for the first time at a surface.

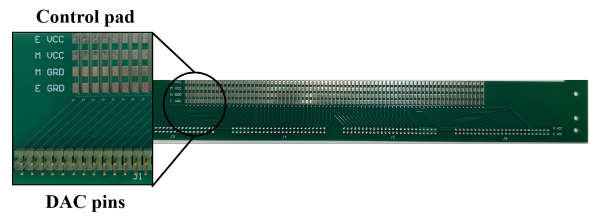

Figure 10: mmWall's FR4 holder/control board.

4 Implementation

We have fabricated and assembled a complete hardware prototype of mmWall, summarized in Fig. 8. mmWall's meta-atoms are fabricated on a 16 by 120 mm *rib* made of Rogers 4003C printed circuit board (PCB) substrate, as shown in Fig. 9. We assemble the PCB and constituent Macom MAVR-000120-1411 varactor diodes[4] and 026011C-1N7 inductors.

In total, we have fabricated 76 ribs, each consisting of 28 vertical meta-atoms. These ribs are mechanically hold together with two perpendicular FR4 panels; one in top and the other in bottom of the structure. The top FR4 also provides control lines as it is shown in Fig. 10. Each rib's control pads are then soldered to the upper holder board, which connects the ribs to a DAC through its microstrip traces and pin headers. The lower holder boards are installed to position and the ribs fixed into these boards. For holding the ribs and FR4 panels steady, a 3D printed enclosure is fabricated that provides a standing support, as shown in Fig. 8(a). The spacing between the adjacent ribs are 2.6 mm, making the dimension of our mmWall prototype 120×197.6 mm. We note that scaling up our prototype with identical ribs and expanded FR4 holder boards is straightforward.

Four 40-channel AD5370 16-bit DACs from Analog Devices allow independent control of both electric and magnetic cells of every mmWall rib. Each DAC supplies a variable

[4] We have modeled this varactor based on its *Simulation Program with Integrated Circuit Emphasis* (SPICE) model (see Appendix, Fig. 17).

0 to 10 V control voltage for each of 40 channels (*i.e.*, one DAC per 20 boards with one channel for U_E and U_M apiece). A laptop is connected to four DACs and listens for control signals from the UE. Once a signal is received, it sends a command to the DACs, which then apply the voltage levels, corresponding to a particular steering angle. Different voltage levels are found from a pre-stored voltage-to-phase look-up table. This control program is written in Microsoft Visual C++, and it can be executed from EnodeB, instead of UE. mmWall hardware, including the DACs, takes 20 μs to reconfigure the beam. The speed of DACs is the key determinant of the total latency, and deploying faster DAC hardware will lower the latency.

5 Evaluation

We begin with field studies that quantify mmWall's SNR gain compared to the best NLoS environment path for both indoor-to-indoor and outdoor-to-indoor links (§5.2). Moreover, we explore the SNR gain and link failure rate under dynamic link conditions. We then evaluate multi-armed beams created by mmWall at various receiver locations (§5.3). We conclude with microbenchmarks to characterize mmWall's steering performance, its support for wide steering angle, angular reciprocity, operation across wide bandwidths, and the impact of the surface size (§5.4).

5.1 Methodology

We conduct evaluations of various indoor and outdoor scenarios. For indoor-to-indoor settings, we place both the receiver (circles in Fig. 11) and transmitter (triangles in Fig. 11) in an office measuring 10×8 m, which includes interior walls, windows, and a server room. Between the three windows, there are two brick walls (black rectangles in Fig. 11). For the outdoor-to-indoor testbed, we locate the transmitter outside the office, approximately $6-7$ m away from the window, while the receiver is inside the office. During the experiments, we place mmWall in front of the window inside the room, and the loss of window is approximately -4 to -5 dB. For each outdoor-to-indoor and indoor-to-indoor experiment, we conduct two sets of experiments, each with a fixed transmitter location and 23 receiver locations. In the first set, the transmitter is perpendicularly facing mmWall and is 6.3 m away (upper subfigures of Fig. 11(a) and left two subfigures of Fig. 11(b)). The second set has the transmitter 6.8 m away from mmWall, and its beam hits the surface at approximately 30° to 40° angle (lower subfigures of Fig. 11(a) and right subfigures of Fig. 11(b)). During the beam search, mmWall steers the angle by the step of 0.5°. For end-to-end performance, we report SNR with a noise floor of 80 dBm.

Near-field experiments. Given that the measured Huygens pattern is likely to deviate from simulated results due to manufacturing tolerances, it is crucial to conduct accurate measurement through near-field experiments and compile a voltage-to-phase look-up table. Specifically, we collect near-field reflection and transmission coefficients of mmWall using two-port Anritsu MS4647B VNA, operating from 70 kHz to 70 GHz, as shown in Fig. 8(b). The Huygens pattern measured from the VNA is shown in Appendix C. To minimize measurement error, we perform a two port calibration before acquiring the data. For data collection, we program the VNA using LabVIEW, which communicates with four DACs through the socket. During the measurement, mmWall is placed in between two waveguide horn antennas that are connected to the VNA. We place two horn antennas closely to mmWall to resemble the near-field simulation. Since the area of mmWall is larger than the aperture of waveguide horns, we collect the pattern on multiple locations of mmWall. In Appendix C, we present a measured Huygens pattern at different locations of mmWall and demonstrate the robustness of mmWall against fabrication variations.

Far-field experiments. A standard mmWave base station is equipped with highly directional phased array antennas and supports an average EIRP range of 55-60 dBm [12, 13] or more. With a 25 dBi transmit horn antenna, the maximum EIRP we achieved is 31 dBm, which is in accordance with FCC rules [14]. We use the same antenna at the receiver but apply a -10 dB correction to reflect typical UE antenna gain. Specifically, to generate mmWave signals, we use off-the-shelf phase-locked loop (PLL) frequency synthesizers ADF4371 with integrated VCO and frequency quadrupler, which quadruples 6.125 GHz VCO signals to 24.5 GHz. At the transmitter, the PLL output power is < -13 dBm, and we use the PLL in conjunction with a variable gain amplifier (VGA) HMC997LC4, which amplifies signals by 18 dBm.

5.2 In-situ Performance

In this section, we evaluate the end-to-end performance of mmWall for indoor and outdoor scenarios.

SNR improvement over the best environment path. To evaluate the effectiveness of mmWall in improving SNR in scenarios with blocked LoS paths, we conduct SNR measurements at multiple transmitter and receiver locations (two locations for the transmitter and 23 locations for the receiver). For each link, the transmitter and receiver (and mmWall if deployed) search for an NLoS path that maximizes the SNR.

Fig. 11 illustrates the measurements taken prior to and following the deployment of mmWall. Specifically, Fig. 11(a) presents the SNRs obtained when the transmitter was positioned towards the window at 0° (upper subfigure) and 30° (lower subfigure) in an indoor testbed. The results of both subfigures show that our indoor testbed has a rich scattering environment, with some receiver locations achieving SNR levels exceeding 25 dB in the absence of mmWall. However,

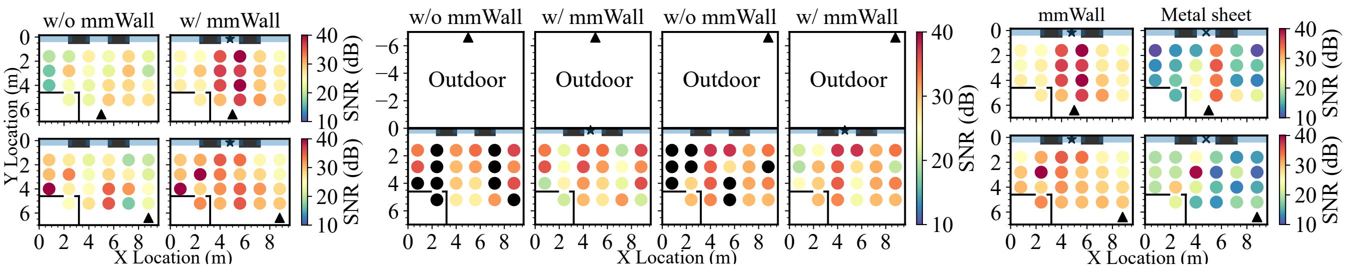

(a) Indoor-to-indoor. **(b)** Outdoor-to-indoor. **(c)** Comparing to a metal sheet

Figure 11: mmWall's SNR improvement over the best NLoS environment path in two scenarios: (a) when both transmitter and receiver are located indoors (*upper*: transmitter facing mmWall perpendicularly; *lower*: transmitter facing 30° away from mmWall) and (b) when the transmitter is located outdoors (*left*: transmitting perpendicularly; *right*: transmitting at a 30° off-angle). We use the following notations: mmWall ★, transmitter ▲, receiver ◯. ● indicates no signal.

receivers located at either end of the room experience SNR levels below 20 dB. With mmWall, all receivers, including the ones in the corner, achieve SNRs of at least 24 dB. Also, the nodes located within mmWall's steering angle of −45° to 45° has SNRs greater than 30 dB. This improvement in SNR is particularly evident in Fig. 12. In Fig. 12 (*left*), we plot a CDF of the best environment SNRs (black curves) alongside the SNRs of mmWall links at the corresponding receiver location (rectangles). Fig. 12 (*center*) shows the CDFs of maximum SNRs between the environment and mmWall links, while Fig. 12 (*right*) shows the CDFs of the SNR gains over the environment path per receiver location. As shown in Fig. 12 (*upper*), mmWall ensures outage-free communication for 91% of receiver locations at 128 QAM [24] mmWave data rates, while only 40-50% of receivers achieve the same rate in the absence of mmWall. Moreover, among 80% of receivers that experience the gain from mmWall, some receive more than a 15 dB SNR boost.

In Fig. 11(b), we present the SNR improvement in outdoor-to-indoor scenarios. Without mmWall, receivers unable to establish an NLoS link through the window experience complete link failure. With mmWall, on the other hand, all receivers achieve SNRs of at least 19 – 20 dB. Fig. 12 (*lower*) shows the CDFs of outdoor-to-indoor SNR improvement. A single mmWall guarantees 64-QAM for almost all receiver locations and a 30 dB SNR boost for 40% of the links. Our results demonstrate that mmWall is highly beneficial for improving mmWave signals quality in the cases of wall blockage.

Deploying multiple mmWalls. To evaluate more than one mmWall, we place another mmWall (downward triangles in Fig. 12) in front of the window on the right side of the room. Fig. 12 (*upper*) demonstrates the SNR gain from deploying two mmWalls for indoor-to-indoor links. Compared to the gain from a single mmWall, an additional mmWall provides ≤ 5 dB SNR gain for some links. As shown in Fig. 12 (*lower*), there is almost no gain from adding an extra mmWall for outdoor-to-indoor links. The results indicate that a single mmWall is sufficient to provide good coverage (at least 128-QAM for reflective and 64-QAM for transmissive links) in a 10×8 m office room. In a static environment another mmWall will not help *if* a mmWall path is already available.

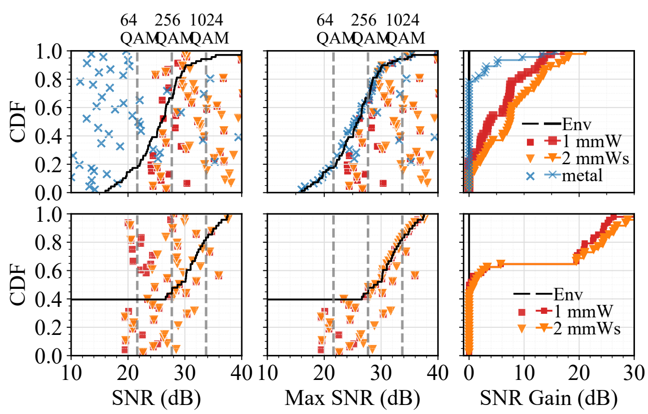

Figure 12: The SNR improvement from the use of one or more mmWalls at various receiver locations in indoor-to-indoor (*upper*) and outdoor-to-indoor (*lower*) scenarios. SNRs collected from a given receiver location are plotted on the same y-axis value (*left*: CDFs of the best environment SNRs in black curves alongside the SNRs of mmWall links at the corresponding receiver location in rectangles. The maximum SNRs between two mmWalls placed in different locations are denoted with downward triangles; *center*: the best available SNRs with or without one or more mmWalls; *right*: the SNR gains attained with one or more mmWalls compared to the best environment path in various Rx locations).

Improving reliability for dynamic links. While a single mmWall delivers good SNRs throughout all receiver locations, it is still possible for blockages to occur on mmWall links. Likewise, even if there is a robust NLoS path present, it can still be blocked. At mmWave frequencies, the indoor environment typically provides three to four strong paths, including the LoS path [23]. Due to the limited number of available paths, an increase in blockages can easily result

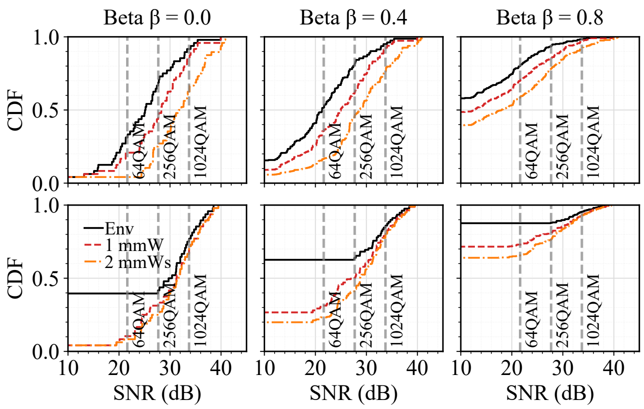

Figure 13: The SNR improvement (multiple mmWalls) for dynamic links (*upper*: indoor-to-indoor; *lower*: outdoor-to-indoor scenarios). β is a blockage probability.

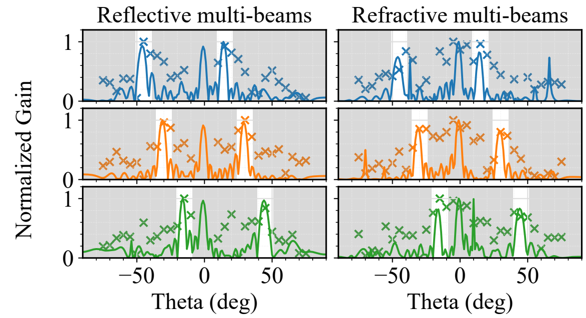

(a) mmWall's multi-armed beam pattern (*upper:* −45/15° degree beam split; *middle:* −30/30° split; *lower:* −15/45° split). Empirical points are denoted ×, with simulation curves.

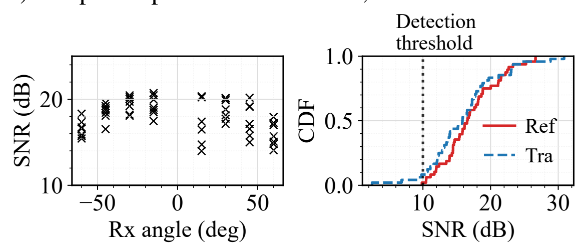

(b) The SNRs of aligned multi-beams (*left:* a fixed distance between the transmitter and mmWall and between the receiver and mmWall; *right:* various Tx and Rx locations in the office setting.)

Figure 14: Evaluation of mmWall's multi-armed beams.

in link failure, which exacerbates when these obstructions are in motion. One of the primary benefits of using one or multiple mmWalls is the enhancement of link reliability. By providing a diverse, strong alternative path, mmWall reduces the probability of link scarcity. In Fig. 13, we demonstrate the SNR gain across various Rx locations as a function of the *blockage probability* β[5] for both environment and mmWall links. In indoor-to-indoor scenarios, a single mmWall and two mmWalls reduce the probability of link failure by a ratio of up to 10% and 20% under 80% path blockage, respectively. For the outdoor testbed, the probability of link failure decreases by 40% for a single mmWall and 45% for two mmWalls under 40% blockage probability. Hence, we conclude that multiple mmWalls are beneficial when channel environments are highly dynamic.

One may argue that deploying a simple reflective metal sheet could help, but mmWall's ability to steer the beam has a significant impact on the extent of coverage. We evaluate the SNRs of links reflected by a 60×60 cm metal sheet, along with the SNRs of links steered by a 10×20 cm mmWall. As shown in Fig. 11(c) (*right*), only 10% of the receivers achieves SNRs above 30 dB, and the remaining 90% have SNRs below 15 dB. It is also worth noting that for a metal sheet, the SNRs depend largely on the location of the receiver and transmitter. In Fig. 11(c) (*right*), only the receivers that are placed and perfectly aligned with the angle of specular reflection achieve a high SNR. In Fig. 12, only 8% of the receivers achieve more than 5 dB SNR gain from the metal sheet. On the other hand, mmWall guarantees at least 25 dB SNRs across all areas. We conclude that, compared to fixed-angle reflection, mmWall links are less sensitive to the location of the transmitter, receiver, and surface, making them much more robust.

[5]A blockage probability is equivalent to a probability of complete link failure for each path. Under various available paths, the blockage probability of one path is independent from the other.

5.3 Multi-armed Beams

We next evaluate mmWall's capability to generate multi-armed beams. Fig. 14(a) presents our measurements on the multi-armed beams, along with simulation results from HFSS. Here, mmWall splits an incident beam into two beams at −45°/15° and steers these multi-beams to −30°/30° and −15°/45°. To measure the beam pattern, we position the transmitter and receiver three meters away from mmWall and record the gain of mmWall as we move the receiver from a −90° to 90° angle with respect to mmWall. Since we did not measure the beam pattern in an anechoic chamber, the received beam interfered with signals reflected off the indoor environment. Despite the interference, we observe that the gain peaks at the angles where mmWall splits the beam. Furthermore, as mmWall steers its multi-armed beams, the measured peaks change accordingly. Our results show a peak at 0° due to leakage that was directly fed from the transmitter to the receiver. Reducing the distance between the transmitter and receiver and/or increasing the size of mmWall will reduce the peak at 0°.

We then measure SNRs as mmWall generates and steers various multi-beams, the beams that are 15° to 120° apart from each other. The distance between the transmitter and mmWall and between the receiver and mmWall are fixed to 2 m. Fig. 14(b) (*left*) reveals that as the beam is split into a wider angle, SNR drops.

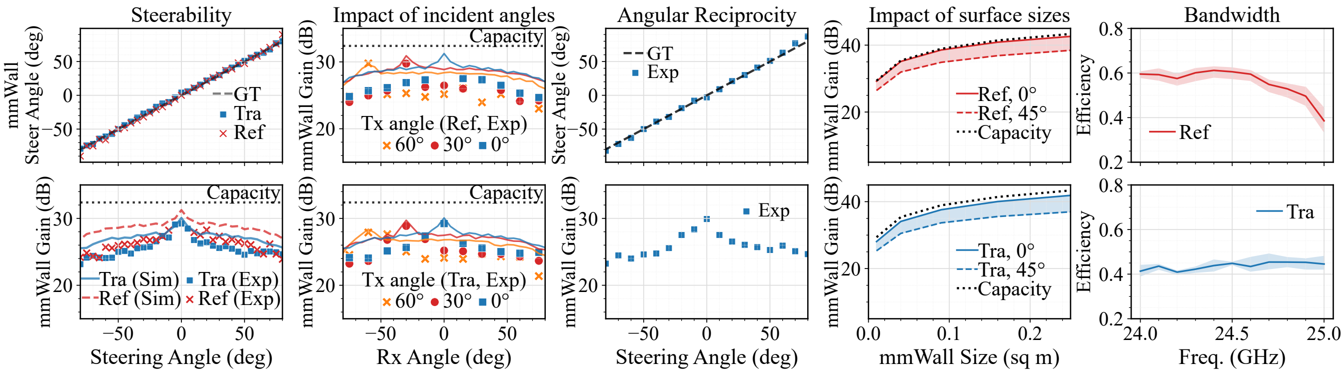

Figure 15: Microbenchmarks evaluating (*left* to *right*:) surface steerability, performance sensitivity of the incident wave angle, angular reciprocity, surface size, and frequency bandwidth. Empirical points are denoted with markers, with simulation curves.

To demonstrate the feasibility of a beam search using multi-armed beams, mmWall again splits the beam into two beams that are 15° to 120° apart from each other. Then it aligns the beam with the receivers at 23 different locations in the room. Fig. 14(b) (*right*) reports the SNRs of mmWall's multi-beam links aligned with various receivers. The results show that more than 90% of multi-beam links achieve SNRs above 10 dB. Considering that no signal is detected in many locations under outdoor-to-indoor settings, 10 dB SNR is enough for the receiver to detect the beam and start the alignment. We conclude that mmWall can generate multi-armed beams that are sufficiently strong to accelerate beam search.

5.4 Microbenchmarks

We now evaluate mmWall's steering performance, its support for wide steering angle, angular reciprocity, operation across wide bandwidths, and the impact of the surface size. The microbenchmark testbed consists of the receiver and transmitter modules that are three meters away from mmWall. Fig. 15 presents both the actual experimental measurements (markers) and simulated results (curves) acquired from HFSS.

Since mmWall does not have an amplifier, the effective aperture A_e is the primary factor that determines its gain. A well-defined relation for the effective aperture in terms of the aperture gain G is $A_e 4\pi/\lambda^2$. We define the aperture gain as our capacity and compare it against our measured mmWall gains in our microbenchmarks. A rigorous analysis on mmWall gain is available in Appendix B.

mmWall controllability. Fig. 15 (*upper first*) presents mmWall's beam alignment accuracy. We place the receiver at 37 locations in our testbed and find the angle that provides the maximum SNR as mmWall sweeps the beam from −80° to 80° angle. During the experiment, the transmitter is facing mmWall at 0° angle. For both reflection and transmission, mmWall accurately steers the beam with at most 3° difference from the groundtruth (GT). Second, we evaluate the effect of a steering angle on the mmWall gain in Fig. 15 (*lower first*). As mmWall increases the steering angle, the gain slowly decreases. Furthermore, reflection provides a slightly higher gain than transmission.

Support for wide steering angle. In this microbenchmark, we evaluate the effect of incident beam angles on the mmWall gain jointly with the steering angle. Here, we move the transmitter to three different locations and the receiver to 37 locations. Fig. 15 (*upper second*) and Fig. 15 (*lower second*) show the impact of incident angles for reflection and transmission, respectively. For both scenarios, increasing the incident beam angle does not greatly reduce the mmWall gain. An important observation is that even with 135° steering angle (*e.g.,* Tx angle at 60° and Rx angle at −75°), mmWall achieves more than 22 dB gain, indicating that mmWall is capable of refracting the beam in a very wide angle.

Angular reciprocity. Once mmWall achieves alignment for the downlink channel, the uplink channel also becomes aligned due to its angular reciprocity. To demonstrate this property, we evaluate the accuracy of uplink beam alignment and the corresponding mmWall gain when downlink alignment is already established. In Fig. 15 (*upper third*), uplink alignment using reciprocity is very accurate and is within an error of 3°. Also, Fig. 15 (*lower third*) shows that all corresponding mmWall gains are above 23 dB using reciprocity.

Operation across wide bandwidths. To demonstrate mmWall's phase coverage across a wide bandwidth, we present our VNA measurements from 20 to 30 GHz. In Fig. 16, each curve indicates the phase response of voltage levels in our lookup table that we compiled at our center frequency, 24.5 GHz. Here, we emphasize three points. First, mmWall provides a full phase coverage from $-\pi$ to π over the 200 MHz 5G mmWave link bandwidth. Second, within 200 MHz bands (highlighted in gray), the phase distributions are mostly constant, allowing improvements over the entirety of these bandwidths. Third, mmWall can operate in the entire 23.5 to 25.5 GHz band, as it provides a wide range of phases there. Hence, mmWall operates over the mmWave 5G band-

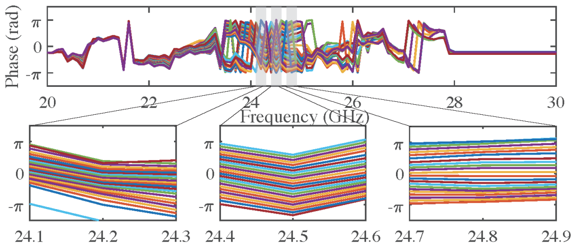

(a) Reflection Γ

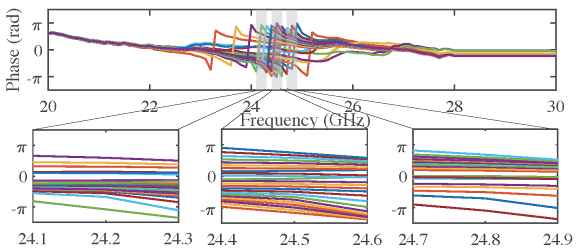

(b) Transmission T

Figure 16: mmWall's phase coverage and consistency (VNA measurement) across different frequencies. The curves indicate the voltage pairs (U_M, U_E) that provide $-180°$ to $180°$ phase shift with the step of $15°$ at 24.5 GHz. The phases are unwrapped across the mmWall's operating bandwidth.

width. More importantly, our meta-atom design goal is to reduce transmission or reflection *loss level* with a full phase coverage. To quantify both magnitude and phase coverage at the same time, we define *efficiency* as $\sum_{\phi=-180}^{180}(Te^{-1j\phi})/360$ where T is a set of points obtained from the near-field transmissive (reflective) Huygens pattern that provides the maximum magnitude for $-180°$ to $180°$ phases. Fig. 15 (*rightmost*) demonstrates that for both reflection and transmission, the efficiency is consistent and declines after 24.9 GHz. Since targeted operational bandwidth for 5G mmWave is 200 MHz, we conclude that mmWall operates within the 5G bandwidth.

Increasing mmWall size. Fig. 15 (*fourth*) shows an increase of simulated gains as mmWall size increases from 10×10 cm to 50×50 cm with $0°$ (for reflection, it is a specular reflection) and $45°$ steering angle. Also, we compare our simulated results against the effective aperture-based capacity. mmWall gains at both $0°$ and $45°$ steering angle increase with increasing surface size, following the capacity trend.

6 Discussion

In this section, we discuss several limitations of mmWall and our potential solutions.

3D beamforming. 3D beamforming technique is beneficial in massive MIMO communications as it sophisticatedly controls the beam in different directions in spatial domain. With mmWall, meta-atoms on the same rib share the voltage level, and therefore it is structured as a 2D linear array. To achieve 3D beamforming, we can simply separate mmWall control lines in the vertical direction. In the future, we will vertically partition mmWall and separately control them.

Tinted window. While mmWave waves propagate through a glass wall with virtually no loss, the penetration loss increases when the glass is metal-coated. Our window has approximately -4 to -5 dB loss with a light tint. If our window is tinted more, SNRs will drop, and this decrease will be equivalent to the increase of penetration loss from a different level of a tint. There is an existing work [45] that measures reflection coefficients and penetration loss for common building materials at mmWave. According to the paper, the penetration loss may increase by more than 20 dB when the window is heavily tinted. With such windows, we can remove the tint of the small area of the window (approx. 0.02 sq m) for mmWall.

Indoor AP as a 5G mmWave relay. An indoor mmWave AP can serve as a relay when the outdoor cell coverage fails to reach indoors. To accomplish this, cellular operators require indoor infrastructure to install an AP capable of receiving 5G signals. This AP then communicates with an internal modem through an Ethernet cable, and the modem wirelessly transmits the signal to the user through Wi-Fi. This deployment is not only costly and time-consuming but also hard to implement. On the other hand, a single mmWall at a fixed location can achieve all three use cases, including 5G outdoor-to-indoor and outdoor-to-outdoor coverage, and indoor WiFi.

7 Conclusion

This paper presents mmWall, the first Huygens metasurface that can reconfigures itself to relay an incoming mmWave beam as either a non-specular "lens" or "mirror." Our prototype steers single- or multi-armed beams at non-specular directions, arbitrarily in real-time. We conduct an extensive evaluation in various indoor and outdoor settings, demonstrating significant SNR improvement, and describe how scaling to even larger sizes is eminently possible.

8 Acknowledgements

This work is supported by the National Science Foundation under grant CNS-1617161, Natural Sciences and Engineering Research Council of Canada (NSERC), Canada Foundation for Innovation (CFI) and Ontario Research Fund (ORF).

References

[1] O. Abari, D. Bharadia, A. Duffield, D. Katabi. Enabling high-quality untethered virtual reality. *USENIX NSDI Symp.*, 531–544, 2017.

[2] O. Abari, H. Hassanieh, M. Rodriguez, D. Katabi. Millimeter wave communications: From point-to-point links to agile network connections. *ACM HotNets Workshop*, 169–175, 2016.

[3] Y. Azar, G. N. Wong, K. Wang, R. Mayzus, J. K. Schulz, H. Zhao, F. Gutierrez, D. Hwang, T. S. Rappaport. 28 GHz propagation measurements for outdoor cellular communications using steerable beam antennas in New York City. *IEEE Intl. Conf. on Comms.*, 5143–5147, 2013.

[4] K. Chen, Y. Feng, F. Monticone, J. Zhao, B. Zhu, T. Jiang, L. Zhang, Y. Kim, X. Ding, S. Zhang, *et al.* A reconfigurable active Huygens metalens. *Advanced materials*, **29**(17), 1606,422, 2017.

[5] L. Chen, W. Hu, K. Jamieson, X. Chen, D. Fang, J. Gummeson. Pushing the physical limits of IoT devices with programmable metasurfaces. *USENIX NSDI Symp.*, 2021.

[6] K. W. Cho, M. H. Mazaheri, J. Gummeson, O. Abari, K. Jamieson. mmwall: A reconfigurable metamaterial surface for mmwave networks. *Proceedings of the 22nd International Workshop on Mobile Computing Systems and Applications*, 119–125, 2021.

[7] L. Dai, B. Wang, M. Wang, X. Yang, J. Tan, S. Bi, S. Xu, F. Yang, Z. Chen, M. D. Renzo, C.-B. Chae, L. Hanzo. Reconfigurable intelligent surface-based wireless communications: Antenna design, prototyping, and experimental results. *IEEE Access*, **8**, 45,913–45,923, 2020.

[8] X. Ding, Z. Wang, G. Hu, J. Liu, K. Zhang, H. Li, B. Ratni, S. N. Burokur, Q. Wu, J. Tan, *et al.* Metasurface holographic image projection based on mathematical properties of Fourier transform. *PhotoniX*, **1**(1), 1–12, 2020.

[9] A. Epstein, G. V. Eleftheriades. Passive lossless Huygens metasurfaces for conversion of arbitrary source field to directive radiation. *IEEE Transactions on Antennas and Propagation*, **62**(11), 5680–5695, 2014.

[10] A. Epstein, G. V. Eleftheriades. Huygens' metasurfaces via the equivalence principle: design and applications. *JOSA B*, **33**(2), A31–A50, 2016.

[11] B. Esmail, H. Majid, Z. Abidin, S. Dahlan, M. Rahim, O. Ayop, *et al.* New metamaterial structure with reconfigurable refractive index at 5G candidate band. *J. Optoelectron Adv M*, **21**(1-2), 101–107, 2019.

[12] FEDERAL COMMUNICATIONS COMMISSION. Ericsson ab pre-nr and nr base radio akrd901059-1.

[13] FEDERAL COMMUNICATIONS COMMISSION. Sfg-aa100dc 5g access unit test report 1 samsung electronics.

[14] FEDERAL COMMUNICATIONS COMMISSION. Title 47, code for federal regulations.

[15] H. Friis. A note on a simple transmission formula. *Proc. of the IRE*, **34**(5), 254–256, 1946.

[16] H. Hassanieh, O. Abari, M. Rodriguez, M. Abdelghany, D. Katabi, P. Indyk. Fast millimeter wave beam alignment. *ACM SIGCOMM Conf.*, 432–445, 2018.

[17] C. L. Holloway, E. F. Kuester, J. A. Gordon, J. O'Hara, J. Booth, D. R. Smith. An overview of the theory and applications of metasurfaces: The two-dimensional equivalents of metamaterials. *IEEE Antennas and Propagation Magazine*, **54**(2), 10–35, 2012.

[18] I. K. Jain, R. Subbaraman, D. Bharadia. Two beams are better than one: Towards reliable and high throughput mmwave links. *ACM SIGCOMM Conf.*, 488–502. New York, NY, USA, 2021.

[19] S. Jog, J. Wang, J. Guan, T. Moon, H. Hassanieh, R. R. Choudhury. Many-to-Many beam alignment in millimeter wave networks. *USENIX NSDI Symp.*, 783–800. Boston, MA, 2019.

[20] Z. Li, Y. Shu, G. Ananthanarayanan, L. Shangguan, K. Jamieson, P. Bahl. Spider: A multi-hop millimeter-wave network for live video analytics. *2021 IEEE/ACM Symp. on Edge Computing (SEC)*, 178–191, 2021.

[21] M. Liu, D. A. Powell, Y. Zarate, I. V. Shadrivov. Huygens' metadevices for parametric waves. *Phys. Rev. X*, **8**(3), 031,077, 2018.

[22] G. R. MacCartney, T. S. Rappaport, S. Sun, S. Deng. Indoor office wideband millimeter-wave propagation measurements and channel models at 28 and 73 GHz for ultra-dense 5G wireless networks. *IEEE Access*, **3**, 2388–2424, 2015.

[23] M. Nemati, B. Maham, S. R. Pokhrel, J. Choi. Modeling RIS empowered outdoor-to-indoor communication in mmWave cellular networks. *IEEE Transactions on Communications*, **69**(11), 7837–7850, 2021.

[24] K. Nishimori, K. Kitao, T. Imai. Interference-based decode and forward scheme using relay nodes in heterogeneous networks. *International Journal of Antennas and Propagation*, **2012**, 2012.

[25] C. Pfeiffer, A. Grbic. Metamaterial Huygens' surfaces: Tailoring wave fronts with reflectionless sheets. *Phys. Rev. Lett.*, **110**, 197,401, 2013.

[26] K. Qian, L. Yao, X. Zhang, T. N. Ng. MilliMirror: 3D printed reflecting surface for millimeter-wave coverage expansion. *ACM MobiCom Conf.*, 2022.

[27] M. E. Rasekh, Z. Marzi, Y. Zhu, U. Madhow, H. Zheng. Noncoherent mmWave path tracking. *ACM HotMobile Workshop*, 13–18, 2017.

[28] N. Shlezinger, G. C. Alexandropoulos, M. F. Imani, Y. C. Eldar, D. R. Smith. Dynamic metasurface antennas for 6G extreme massive MIMO communications. *IEEE Wireless Comms.*, **28**(2), 106–113, 2021.

[29] D. R. Smith, J. B. Pendry, M. C. Wiltshire. Metamaterials and negative refractive index. *Science*, **305**(5685), 788–792, 2004.

[30] S. Sur, I. Pefkianakis, X. Zhang, K.-H. Kim. WiFi-assisted 60 GHz wireless networks. *ACM MobiCom Conf.*, 28–41. New York, NY, USA, 2017.

[31] X. Tan, Z. Sun, D. Koutsonikolas, J. M. Jornet. Enabling indoor mobile millimeter-wave networks based on smart reflect-arrays. *IEEE INFOCOM Conf.*, 270–278, 2018.

[32] W. Tang, M. Z. Chen, X. Chen, J. Y. Dai, Y. Han, M. Di Renzo, Y. Zeng, S. Jin, Q. Cheng, T. J. Cui. Wireless communications with reconfigurable intelligent surface: Path loss modeling and experimental measurement. *IEEE Trans. on Wireless Comms.*, **20**(1), 421–439, 2021.

[33] W. Tang, X. Chen, M. Z. Chen, J. Y. Dai, Y. Han, M. Di Renzo, S. Jin, Q. Cheng, T. J. Cui. Path loss modeling and measurements for reconfigurable intelligent surfaces in the millimeter-wave frequency band. *IEEE Trans. on Comms. (Early Access)*, 2022.

[34] A. Vallecchi, E. Shamonina, C. J. Stevens. Analytical model of the fundamental mode of 3D square split ring resonators. *J. of Applied Physics*, **125**(1), 014,901, 2019.

[35] E. Violette, R. Espeland, R. DeBolt, F. Schwering. Millimeter-wave propagation at street level in an urban environment. *IEEE Trans. on Geoscience and Remote Sensing*, **26**(3), 368–380, 1988.

[36] X. Wang, P.-Y. Qin, A. T. Le, H. Zhang, R. Jin, Y. J. Guo. Beam scanning transmitarray employing reconfigurable dual-layer huygens element. *IEEE Transactions on Antennas and Propagation*, **70**(9), 7491–7500, 2022.

[37] T. Wei, A. Zhou, X. Zhang. Facilitating robust 60 GHz network deployment by sensing ambient reflectors. *USENIX NSDI Symp.*, 213–226, 2017.

[38] Z. Wu, Y. Ra'di, A. Grbic. Tunable metasurfaces: A polarization rotator design. *Physical Review X*, **9**(1), 011,036, 2019.

[39] Y. Xing, F. Vook, E. Visotsky, M. Cudak, A. Ghosh. Raytracing-based system performance of intelligent reflecting surfaces at 28 GHz. *IEEE Intl. Conf. on Comms.*, 498–503, 2022.

[40] C. Xue, Q. Lou, Z. N. Chen. Broadband double-layered huygens' metasurface lens antenna for 5g millimeter-wave systems. *IEEE Transactions on Antennas and Propagation*, **68**(3), 1468–1476, 2019.

[41] K. Ying, Z. Gao, S. Lyu, Y. Wu, H. Wang, M.-S. Alouini. GMD-based hybrid beamforming for large reconfigurable intelligent surface assisted millimeter-wave massive MIMO. *IEEE Access*, **8**, 19,530–19,539, 2020.

[42] R. I. Zelaya, W. Sussman, J. Gummeson, K. Jamieson, W. Hu. LAVA: fine-grained 3D indoor wireless coverage for small IoT devices. *ACM SIGCOMM Conf.*, 123–136, 2021.

[43] L. Zhang, X. Q. Chen, S. Liu, Q. Zhang, J. Zhao, J. Y. Dai, G. D. Bai, X. Wan, Q. Cheng, G. Castaldi, *et al.* Space-time-coding digital metasurfaces. *Nature Communications*, **9**(1), 1–11, 2018.

[44] H. Zhao, R. Mayzus, S. Sun, M. Samimi, J. K. Schulz, Y. Azar, K. Wang, G. N. Wong, F. Gutierrez, T. S. Rappaport. 28 GHz millimeter wave cellular communication measurements for reflection and penetration loss in and around buildings in New York City. *IEEE Intl. Conf. on Comms.*, 5163–5167, 2013.

[45] H. Zhao, R. Mayzus, S. Sun, M. Samimi, J. K. Schulz, Y. Azar, K. Wang, G. N. Wong, F. Gutierrez, T. S. Rappaport. 28 ghz millimeter wave cellular communication measurements for reflection and penetration loss in and around buildings in new york city. *2013 IEEE International Conference on Communications (ICC)*, 5163–5167. IEEE, 2013.

A Unit Cell Electromagnetic Analysis

We now present a full mathematical analysis of mmWall's unit cells. Since electromagnetic fields are naturally continuous and will not change the propagation characteristics by itself, we artificially introduce electric and magnetic surface currents $(\vec{J_s}, \vec{M_s})$ from the electric and magnetic meta-atoms, enforcing a field discontinuity:

$$\vec{J_s} = \hat{n} \times [H_t - H_i],\ \vec{M_s} = -\hat{n} \times [E_t - E_i] \tag{4}$$

where $\hat{n}$ is a unit normal. The average tangential field applied on the meta-atom pair induces $(\vec{J_s}, \vec{M_s})$. To induce suitable surface currents, we need a proper surface impedance for each meta-atom:

$$\begin{aligned} \hat{n} \times [E_{avg}] &= Z_e \vec{J_s} = Z_e \hat{n} \times [H_2 - H_1] \\ \hat{n} \times [H_{avg}] &= Y_m \vec{M_s} = -Y_m \hat{n} \times [E_2 - E_1] \end{aligned} \tag{5}$$

where Z_e is the electric surface impedance and Y_m is the magnetic surface admittance equivalent to $1/Z_m$. In fact, the electric and magnetic meta-atoms are each described by a surface impedance of LC oscillating circuit containing inductance L and capacitance C. Mathematically, we can formulate the surface impedance of the electric and magnetic meta-atom as

$$Z_e = \left(\frac{2\pi f C_e - 1}{(2\pi f)^2 L_e C_e}\right) j,\ Y_m = \left(\frac{1 - (2\pi f)^2 L_m C_m}{2\pi f C_m}\right) j \tag{6}$$

where f indicates the resonant frequency. Each meta-atom behaves as an LC circuit when its resonant frequency f matches the frequency of the incident wave. Mathematically, the resonant frequency is equivalent to $f = (2\pi\sqrt{LC})^{-1}$.

Given Z_e and Y_m, we can formulate the transmission coefficient T and reflection coefficient Γ of a meta-atom pair:

$$T = \frac{4 - Y_m \cdot Z_e}{(2 + Y_m \cdot \eta)(2 + Z_e/\eta))},\ \Gamma = \frac{2(Z_e/\eta - Y_m \cdot \eta)}{(2 + Y_m \cdot \eta)(2 + Z_e/\eta)} \tag{7}$$

where η is the wave impedance in free space. Hence, by changing the surface impedance (Z_e, Y_m), we precisely control the phase of the coefficients, creating an arbitrary phase shift on the incident wave [10].

The excitation of the electric and magnetic surface currents, or, equivalently, the values of Z_e and Y_m is tuned by changing the capacitive or inductive loading of the meta-atoms as shown in Eq. (6). Hence, to make HMS reconfigurable, we load a voltage-controlled capacitor, varactor diode, on each meta-atom. By applying voltage across each varactor, we can arbitrary change the surface impedance, or equivalently, the phase of the transmission or reflective coefficient.

Since the electric and magnetic meta-atoms are superimposed on the surface, we dissect the equivalent circuit model for the electric and magnetic meta-atom individually.

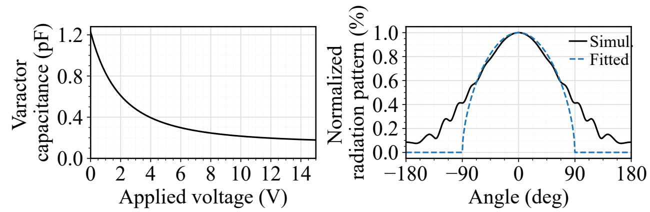

Figure 17: *Left:* C_{var} as the voltage applied to varactor changes, modeled with SPICE simulation; *Right:* mmWall element normalized beam pattern $F(\theta)$ simulated with HFSS and fitted function.

A.1 Magnetic Meta-atom

In this section, we provide the formulas for the magnetic meta-atom's capacitance and inductance discussed in §3.1.2. First, we define the inductance of a circular metallic loop L_{loop} as

$$L_{loop} = \mu_0 R \left(log\left(\frac{8R_m}{t+w} - \frac{1}{2}\right)\right), \tag{8}$$

where R is a mean radius, and μ_0 is free-space permeability. Since there is a gap on the top of a metallic loop, the inductance of our magnetic meta-atom can be calculated as

$$L_m = p_m L_{loop} = \left(1 - \frac{g}{2\pi R}\right) L_{loop}, \tag{9}$$

where g is a length of the gap. Now, we present the calculation of C_m. First, the gap in the metallic loop creates a parallel-plate capacitance as follow:

$$C_{gap} = \varepsilon \frac{wt}{g} + \varepsilon(t + w + g), \tag{10}$$

where w is the width of the loop, and t is the thickness of the copper. Here, $\varepsilon = \varepsilon_0 \varepsilon_{eff}$ where ε_0 is free-space permittivity, and ε_{eff} is effective permittivity, which can be calculated as

$$\varepsilon_{eff} = \frac{\varepsilon_r + 1}{2} + \left(\frac{\varepsilon_r - 1}{2}\right)\left(\frac{1}{\sqrt{(1 + 12t/e)}}\right) \tag{11}$$

where ε_r is the permittivity of the substrate. Second, there is a capacitance induced by the metallic ring itself:

$$C_{surf} = \frac{2\varepsilon(t+w)}{\pi} ln\left(\frac{4R}{g}\right) \tag{12}$$

Lastly, the varactor diode adds the capacitance as discussed in §3.1.2. We have modeled our varactor, of Macom MAVR-000120-1411, based on its *Simulation Program with Integrated Circuit Emphasis* (SPICE) model and demonstrate our simulated C_{var} values in the left subfigure of Fig. 17. Then, we formulate C_m according to Eq. (1). Finally, we model the circuit diagram as a series impedance where the series impedance itself corresponds to the surface impedance $Z_m = 1/Y_m$.

	Radius R (mm)	Gap g (mm)	Width w (mm)
Ele.	0.8831	0.1016	0.3048
Mag.	0.7907	0.2794	0.3048

Table 1: mmWall design parameters.

A.2 Electric Meta-atom

Now, we provide the capacitance and inductance calculation for the electric meta-atom. First, we formulate the inductance of a half-circle ring L_{curve} as follow:

$$L_{curve} = (p_e L_{circle})/2 = \frac{1}{2}\left(\left(1-\frac{g}{2\pi R_m}\right)L_{circle}\right). \quad (13)$$

Based on [11], we compute the the inductance of the strip as

$$L_{strip} = \mu_0 l/4\pi\Big[2\sinh^{-1}(\tfrac{l}{w}) + 2(\tfrac{1}{w})\sinh^{-1}(\tfrac{w}{l}) - \frac{2(w^2+l^2)^{1.5}}{3lw^2} + \tfrac{2}{3}(\tfrac{l}{w})^2 + \tfrac{2}{3}(\tfrac{w}{l})\Big] \quad (14)$$

where l is the length of strip, which is equivalent to $2R_m$, and w is the width of the trace. We then combine all inductance values into L_e as

$$L_e = (L_{curve}/2) + L_{strip} \quad (15)$$

The formulas for the gap capacitance and surface capacitance for the electric meta-atom are the same as the magnetic meta-atom, and we define C_e according to Eq. (2). Finally, the surface impedance of the electric meta-atom corresponds to a shunt impedance.

A.3 Design Parameters

We present the exact values for our design parameters, including radius R, gap g, and width w of the magnetic and electric meta-atom, in Table. 1. Also, the voltage levels applied to the magnetic and electric meta-atoms for different phase shifts are shown in Fig. 18. The y-axis indicates the voltage level, and the x-axis is different ribs. Specifically, Fig. 18(a) demonstrates a set of U_M and U_E required for $-30°$, $-15°$, $0°$, $15°$, and $30°$ transmissive steering. Similarly, Fig. 18(b) shows the voltages values required for reflective steering.

B Path Loss Model

This section presents a standard path loss model calculation largely following the development in prior similar efforts targeting lower frequencies [32], useful for our purposes to establish the basic feasibility of our design prior to hardware fabrication and full-scale evaluation.

First let us assume that a transmitter directly communicates with a receiver. According to the Friis formula [15], the power

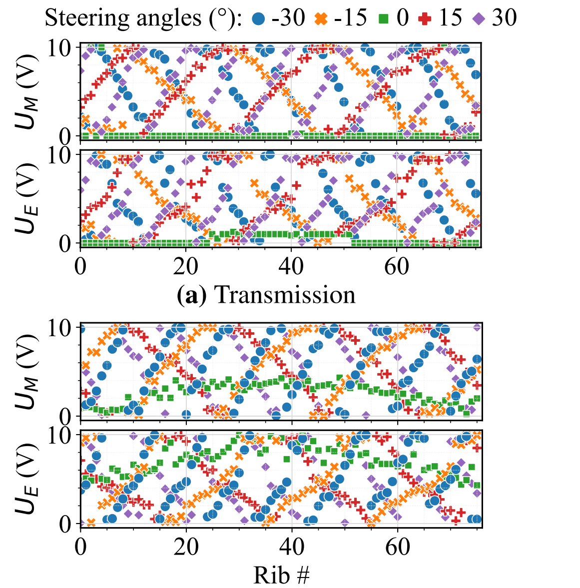

Figure 18: *Upper:* a set of voltage levels applied to the magnetic and electric meta-atoms U_M and U_E for transmissive steering; *Lower:* voltage levels applied for reflective steering.

intercepted by the receiving antenna with effective aperture Ae_R and distance between transmitter and receiver d is:

$$P_i = S_R Ae_R = \left(\frac{P_T}{4\pi d^2}G_T\right)Ae_R \quad (16)$$

where S_R is the received power density, and G_T is the peak gain of the transmitting antenna. Since the effective aperture $Ae_R = \frac{\lambda^2}{4\pi}G_R$ where G_R denotes the gain of the receiving antenna, we rewrite Eq. (16) as

$$P_i = \left(\frac{P_T}{4\pi d^2}G_T\right)\left(\frac{\lambda^2}{4\pi}G_R\right) = P_T G_T G_R\left(\frac{\lambda}{4\pi d}\right)^2. \quad (17)$$

Now we consider a transmitter communicating with the receiver via mmWall. Given Eq. (17), we formulate the power the nm^{th} meta-atom captures from the transmitter as

$$P^i_{nm} = P_T G_T G_w\left(\frac{\lambda}{4\pi d_{i,nm}}\right)^2, \quad (18)$$

where G_w denotes the gain of the meta-atom in the direction of the transmitter, and $d_{i,nm}$ is the distance between the transmitter and nm^{th} meta-atom. Similarly, we can calculate the power received by the receiving antenna from the nm^{th} meta-atom as:

$$P_{R,nm} = P^s_{nm} G_R G_w\left(\frac{\lambda}{4\pi d_{s,nm}}\right)^2, \quad (19)$$

where G_w is the meta-atom gain scattered in the direction of the receiver, $d_{s,nm}$ is the distance between nm^{th} meta-atom to the receiver, P^s_{nm} is the power applied by each meta-atom, and $P^s_{nm} = P^i_{nm}\varepsilon$. Here, ε accounts for the limited efficiency of meta-atom and insertion losses associated with components. To simplify the formula, we assume $\varepsilon = 1$. To calculate the power from the transmitter to the receiver, we then combine Eqs. (18) and (19):

$$P_{R,nm} = P_T G_T G_R \frac{G_w G_w}{d^2_{i,nm} d^2_{s,nm}} \left(\frac{\lambda}{4\pi}\right)^4 \tag{20}$$

Here, we emphasize that in the link budget, we must calculate the gain of mmWall twice, one for receiving and another for transmitting. Hence, Eq. (20) has two G_w. Since mmWall consists of a large array of meta-atoms, we can formulate the total received power as a sum of the received powers from all meta-atoms as

$$P_R = \left|\sum_{n=1}^{N}\sum_{m=1}^{M} C_{nm}\sqrt{P_{R,nm}}e^{j\phi_{nm}}\right|^2, \tag{21}$$

where $C_{n,m}$ denotes the transmission or reflection coefficient of the nm^{th} meta-atom, and the phase $\phi_{nm} = 2\pi(d_{i,nm} + d_{s,nm})/\lambda$. In a lens mode $C_{n,m} = T_{n,m}$, and in a mirror mode $C_{n,m} = \Gamma_{n,m}$. We already defined $T_{n,m}$ and $\Gamma_{n,m}$ in eq. Eq. (7). Finally, we write the total received power as:

$$P_R = P_T G_T G_R \left(\frac{\lambda}{4\pi}\right)^4 \left|\sum_{n=1}^{N}\sum_{m=1}^{M} C_{nm}\frac{\sqrt{G_w G_w}}{d_{i,nm}d_{s,nm}}e^{j\phi_{nm}}\right|^2. \tag{22}$$

However, the meta-atom gain G_w is unknown. Thus, we re-define G_w as a power radiation pattern from each meta-atom, which is equivalent to $GF(\theta_{nm})$. G is a gain that depends on the physical area (*i.e.* the effective aperture) of the meta-atom, and $F(\theta_{nm})$ is the normalized power radiation pattern. Based on the effective aperture formula, $G = (4\pi/\lambda^2)Ae_{nm} = (4\pi/\lambda^2)(xy)$ where x and y are vertical and horizontal meta-atom spacing, respectively. Unlike traditional antennas with $x = y = \lambda/2$, our meta-atom has $x = \lambda/4.8$ and $y = \lambda/3.4$. Moreover, $F(\theta_{nm})$ defines the variation of the power radiated or received by a meta-atom:

$$F(\theta) = \begin{cases} cos^q(\theta) & \theta \in [0, \pi/2] \\ 0 & \theta \in [\pi/2, \pi] \end{cases} \tag{23}$$

where θ are the angle from the meta-atom to a certain transmitting or receiving direction. In the right subfigure of Fig. 17, we present a simulated mmWall element beam pattern $F(\theta_{nm})$ as well as the curve fitted with Eq. (23). Based on our curve fit, $q = 0.5611$.

Far-field beamforming. In the far-field, we can approximate $d_{s,nm} = d_s$ and $d_{i,nm} = d_i$ since d_i and d_s are much greater than the distance between different meta-atoms. However, we do not approximate $d_{s,nm} = d_s$ and $d_{i,nm} = d_i$ for the phase ϕ_{nm}.

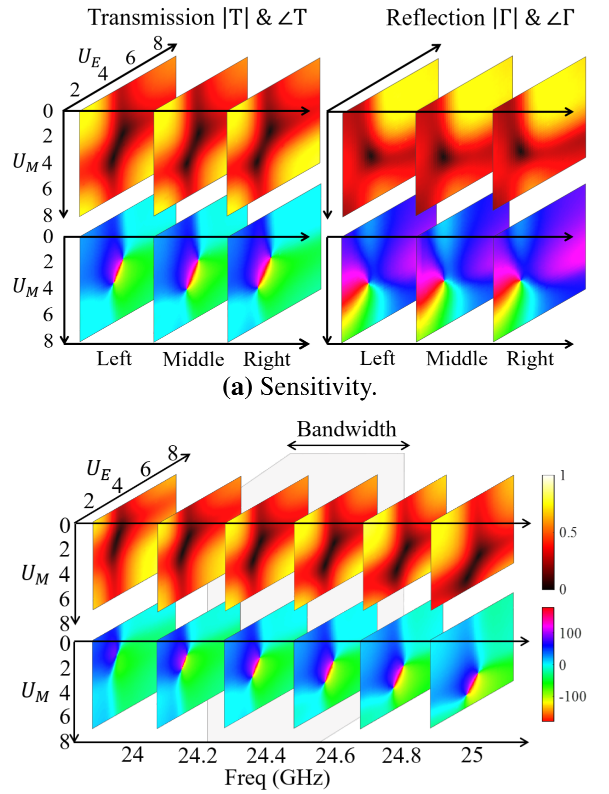

(a) Sensitivity.

(b) Bandwidth.

Figure 19: Meta-atom microbenchmark

Then, we can simplify Eq. (22) as:

$$P_R = P_T G_T G_R \left(\frac{Ae_{nm}}{4\pi d_i d_s}\right)^2 F(\theta_i)F(\theta_s)\left|\sum_{n=1}^{N}\sum_{m=1}^{M} C_{nm}e^{j\phi_{nm}}\right|^2 \tag{24}$$

This indicates that we can maximize the received power by configuring each meta-atom's $\angle C_{nm}$ to $-\phi_{nm}$. Finally, the path loss of a correctly reconfigured mmWall as:

$$L^{-1}_{mmWall} = (\frac{xy}{4\pi d_i d_s})^2 F(\theta_i)F(\theta_s)\left|\sum_{n=1}^{N}\sum_{m=1}^{M} |C_{nm}|\right|^2 \tag{25}$$

Since $0 < |C_{nm}| < 1$ for both transmissive and reflective mode, increasing the number of meta-atoms N and/or M reduces the path loss. Assuming $|C_{nm}|$ is close to 1, the path loss of mmWall is proportional to $1/(NM)^2$. While increasing the element spacing x and y seems to reduce the loss, it is not always true because $|C_{nm}|$ decreases when x and y increase due to increasing coupling between adjacent meta-atoms.

C Meta-atom controllability and sensitivity

We present the Huygens pattern measured from the VNA in Fig. 19(a). We measure the near-field Huygens pattern in three different areas of mmWall to evaluate its sensitivity against fabrication variation. For all three areas, we observe a 360-degree phase variation with high magnitude for both transmission and reflection. Moreover, the patterns do not vary across the different areas of the surface, signifying that manufacturing tolerance do not greatly affect mmWall's near-field performance. We also demonstrate the Huygens pattern across mmWall's operating bandwidth in Fig. 19(b). Within the 200 MHz bandwidth, the pattern is consistent.